

# Measuring and analyzing defects of Additive Manufactured Ti-6Al-4V Specimens through Image Segmentation

Ro'i Lang<sup>1a</sup>, Or Haim Anidjar<sup>b,h</sup>, Sahar Slonimsky<sup>a</sup>, Chen Hajaj<sup>c</sup>, Oz Golan<sup>d</sup>, Carmel Matias<sup>e</sup>, Alex Diskin<sup>f</sup>, Strokin Evgeny<sup>g</sup>, Mor Mega<sup>a</sup>

<sup>a</sup>Department of Mechanical Engineering and Mechatronics  
Fracture and Fatigue Research Laboratory  
Ariel University  
4077625, Ariel, Israel

<sup>b</sup>Department of Computer Software & Engineering  
Ariel University  
4077625, Ariel, Israel.

<sup>c</sup>Department of Industrial Engineering and Management  
Ariel University  
4077625, Ariel, Israel.

<sup>d</sup>Afeka Center for Materials and Processes Engineering  
Afeka Tel-Aviv Academic College of Engineering  
6998812, Tel Aviv, Israel.

<sup>e</sup>Aviation Group, Engineering & Development Center  
Fatigue and Damage Tolerance Dept.  
Israel Aerospace Industries (IAI)  
70100 Ben-Gurion International Airport, Israel.

<sup>f</sup> Material Engineering & Technology Development Dept.  
Aviation Group  
Israel Aerospace Industries (IAI)  
70100 Ben-Gurion International Airport, Israel.

<sup>g</sup> Research & Development  
Technion – Israel Institute of Technology  
3200003, Haifa, Israel.

<sup>h</sup> School of Computer Science  
College of Management  
7579806, Rishon Le'Tzion, Israel.

---

<sup>1</sup>e-mail: lang.roi@gmail.com

# Abstract

The use of additive manufacturing has increased significantly in recent years, particularly in the aerospace industry. However, AM materials often exhibit defects that adversely impact fatigue performance. This study examines the geometric and morphological features of critical defects observed in Ti-6Al-4V specimens.

A framework for automatic fatigue failure analysis through computer vision is proposed. An AI-based tool was trained to identify critical defects, measure their proximity to the surface, and quantify 14 geometric and morphological features. The findings indicate that surface proximity is the most influential factor in fatigue life classification, with defects near the surface exerting a negative impact on performance. No clear trend was observed in defect morphology beyond a certain surface distance. For lack-of-fusion defects classified as critical, the  $X$ -parameter model was applied and a correlation of  $R^2 = 0.91$  with the measured CTF was obtained.

**Keywords:** Additive Manufacturing, Deep Learning, Fatigue Failure, Image Segmentation, Fractography.

# 1 INTRODUCTION

In recent years, there has been a surge of interest in Additive Manufacturing (AM)<sup>1</sup> across various industries, particularly in aerospace.<sup>2,3</sup> Compared to traditional manufacturing methods, AM techniques can produce parts with complex geometries and low buy-to-fly ratios. However, several studies, such as Edwards & Ramulu,<sup>4</sup> or Leuders et al.,<sup>5</sup> have shown that while the quasi-static properties and crack propagation behavior of AM materials are comparable to those of standard materials, their fatigue life is not. Post-processing techniques, including machining and Hot Isostatic Pressing (HIP)<sup>6</sup>, can enhance the fatigue performance of AM materials by removing surface defects and sealing internal pores.<sup>7-9</sup> However, fatigue performance still depends on specific printing parameters,<sup>10,11</sup> print orientations,<sup>12</sup> heat treatments,<sup>8</sup> and complementary processes (such as HIP or surface treatments),<sup>13,14</sup> making it highly reliant on quality assurance measures to eliminate defects to achieve the levels observed in conventionally manufactured materials. Consequently, the use of AM for manufacturing key structural elements is not yet mature due to the lack of efficient, generic quality control methods for economically detecting defects.

Defects in AM include lack of fusion (LOF), inclusions, and poor surface quality.<sup>10,15</sup> Additionally, due to rapid cooling during manufacturing, residual stresses are common. These phenomena have a negative effect on fatigue performance. Currently, there are no regulatory guidelines for disqualifying defective AM parts during the manufacturing process. To establish mechanical characterizations for critical defects that warrant part dismissal, extensive studies of fatigue failure are required, linking post-mortem fractographic analyses to measured fatigue life. Insights into the geometrical and morphological characteristics of failure sources, as well as crack formation and propagation, can be gained through fractographic examination of fractured surfaces using a scanning electron microscope (SEM).<sup>16</sup>

The types of defects within an AM part may be divided into three main types of fatigue crack initiation sites, namely, LOF defects, surface defects, or 'random' where no specific initial defect is observed but the location of initial fatigue failure is clear. An example of each failure source type is presented in Fig. 1. The initiation sites act as stress concentration surfaces where fatigue cracks may form.<sup>17</sup> While LOF and surface defects are clearly visible in SEM scans of the fractured surface, as shown in Fig. 1A and 1B, respectively, 'random' initiation sites, as shown in Fig. 1C, are not apparent defects and are likely fatigue cracks originating at grain boundaries.<sup>18</sup>

Various semi-empirical models may be found in the literature that relate defect characteristics to fatigue properties. Murakami et al.<sup>19-21</sup> proposed a method for predicting the fatigue

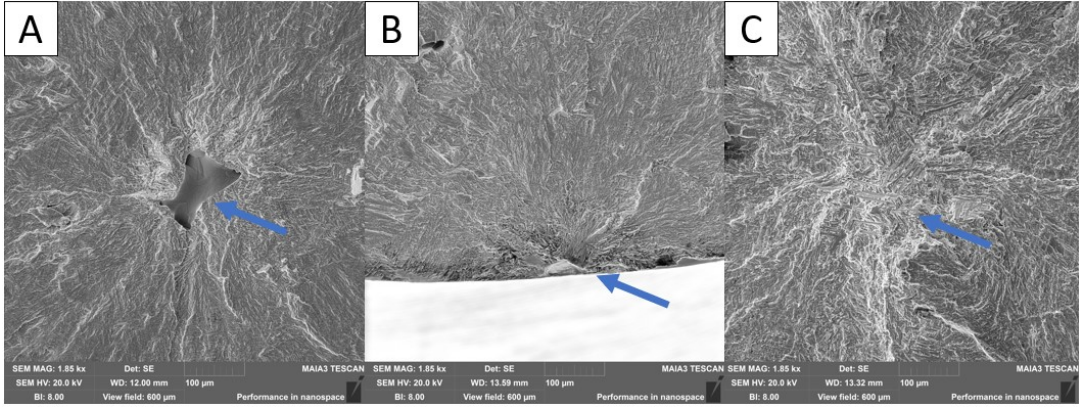


Figure 1: **Examples of SEM scans of fatigue crack initiation sites: (A) Lack of fusion (LOF) initiation site, (B) Fatigue crack originating from a surface defect, (C) A 'random' initiation site, likely originating at grain boundaries.**

limit and fatigue life of metal materials with defects as

$$\sigma_w = \frac{C(HV + 120)}{(\sqrt{area})^{1/6}} \quad (1)$$

where  $\sigma_w$  denotes the rotating bending or tension-compression fatigue limit,  $C$  is defined as 1.43 for surface defects and 1.56 for subsurface defect,  $HV$  is the Vickers Hardness, and  $\sqrt{area}$  is the square root of the effective area of the defect. The effective area is determined as the convex area when the defect's diameter exceeds its distance to the surface of the specimen. For defects situated closer to the surface, the effective area encompasses the projection of the defect onto the plane perpendicular to the direction of the maximum principal stress. The fatigue life of a specimen may then be calculated using

$$\frac{da}{dN} = C^* \left( \frac{\sigma}{\sigma_w} - 1 \right)^{m^*} a^{n^*} . \quad (2)$$

where  $da/dN$  is the crack propagation rate,  $\sigma$  is the applied stress amplitude,  $a$  represents the defect size in terms of  $\sqrt{area}$ . The parameters  $C^*$ ,  $m^*$ , and  $n^*$  were obtained for various steels, cast irons and alloys empirically and are equal  $10^{-4}$ , 2 and 1, respectively.<sup>20</sup> It is crucial to recognize that other defect attributes, such as their proximity to the surface and shape—where the former is considered in  $C$  in a binary manner, while the latter is not considered—could potentially influence fatigue crack initiation. It may be noted that, even if fatigue limit, S-N curve or fatigue propagation rate may be estimated for a particular defect, discerning the criticality of a detected defect and identifying its most crucial features for quality control assessment remains challenging.

Zhu et al.<sup>22</sup> introduced the  $Z$ -parameter model to relate defect geometry, stress amplitude,

and fatigue life, expressed as

$$Z = Y\sigma_a (\sqrt{\text{area}})^{-1/6} D^\beta \quad (3)$$

where  $Y$  is the shape factor related to the fatigue source morphology,  $\sigma_a$  is the applied stress amplitude, and  $D$  is the location factor, defined as  $(d-h)/d$ , with  $d$  being the specimen diameter and  $h$  the distance between the defect center and the outer surface. The parameter  $D$  ranges from 0.5 (center) to 1 (surface), the parameter  $\beta$  is a fitting parameter based on  $Z - N_f$  data, where  $N_f$  is the number of cycles to failure (CTF). This model reduces variability in fatigue life data, emphasizing the effects of stress, defect location, size, and shape.

Later, Hu et al.<sup>23</sup> proposed the  $X$ -parameter model to also include defect circularity as

$$X = \frac{\sigma_a (\sqrt{\text{area}})^{-1/6} D^\beta}{C^\alpha} \quad (4)$$

where  $C$  represents defect circularity, with values close to 1 for circular defects, and decreasing as the defect shape becomes more irregular. Here, the parameter  $\alpha$  is an additional fitting parameter.

While the Murakami, Z-parameter, and  $X$ -parameter models provide valuable insights and simplifications for predicting fatigue life based on defect size and location, they are phenomenological and require extensive testing. In Powder Bed Fusion (PBF) techniques, materials are produced using powders with varying properties, leading to inconsistent defect types and characteristics, which these models may struggle to capture effectively.

Recently, purely data-driven approaches have shown great potential in addressing high-dimensional data and regression challenges, making them a valuable tool for researchers studying complex fatigue processes and assessing fatigue performance. Machine Learning (ML) algorithms are renowned for their ability to detect intricate patterns in complex datasets.<sup>24</sup> Additionally, these algorithms are instrumental in assessing the impact of individual input parameters on model outcomes and establishing mathematical criteria, curves, or trends. In Ref.,<sup>25</sup> a review of ML-based methods for fatigue life prediction of AM metals is presented, and the challenges and opportunities facing researchers today are discussed. Bao et al.<sup>26</sup> investigated machine learning (ML) techniques for predicting the fatigue life of AM metals, an SVM model was used in that study to assess the impact of defect characteristics on the high-cycle fatigue (HCF) life of SLM Ti-6Al-4V, achieving predictions with less than 4% error from actual measurements. Li et al.<sup>27</sup> developed a data-driven framework to evaluate defect criticality in Laser Powder Bed Fusion (L-PBF) 17-4 PH stainless steel specimens concerning fatigue life. They measured geometrical attributes from 192 critical defects identified postmortem. The ML analysis utilized support vector regression (SVR) to correlate defect features with the CTF

of the specimen. A total of 14 features were used, comprising 8 size-related features such as defect area and perimeter, 5 morphology-related features such as eccentricity and circularity, and the distance to the surface. The results showed high feature correlations and accurate fatigue life predictions, especially in small, consistent datasets. Peng et al.<sup>28</sup> identified applied stress, projected defect area, defect location, and defect morphology as the four key parameters affecting the fatigue life of AM metals. They developed a fatigue life prediction method using the XGBoost algorithm,<sup>29</sup> which was compared with predictions from Murakami<sup>19</sup> and the  $X$ -parameter model<sup>23</sup> with more accurate predictions made with the ML algorithms.

A crucial factor in determining the effectiveness of ML analyses is the size of the dataset used for training the models. Larger datasets are typically more effective at capturing real-world patterns, leading to more accurate models, as they encompass greater variability, reduce over-fitting, enhance statistical significance, and improve the handling of outliers<sup>30</sup>. However, creating such extensive datasets requires detailed manual fractographic analysis, which is significantly time-consuming. Implementing Deep Learning and computer vision<sup>31</sup> tools in fractography is a relatively new field. Tsopanidis et al.<sup>32</sup> employed a VGG16 model in a U-net architecture<sup>33,34</sup> for segmenting intergranular and transgranular fractures in ceramic materials, achieving a total mean Intersection over Union (IoU) of over 91% for two different materials. Similarly, Tang et al.<sup>35</sup> compared the effectiveness of different segmentation models in segmenting multiple morphological features, achieving an mean IoU of 59.7%. Another fractographic challenge, image classification, was explored by Bastidas-Rodriguez et al.,<sup>36</sup> who used Deep Learning models to classify images with different failure mechanisms, achieving an accuracy of 87.1%.

One of the primary objectives of this research is to develop a computer vision framework for the automatic fractographic analysis of metal AM high-cycle fatigue (HCF) specimens, thereby streamlining future research efforts. In Ref.,<sup>37</sup> a framework for detecting fatigue crack initiation sites in AM materials was proposed. In this study, the algorithm for measuring the distance from the initiation site to the surface is further enhanced. Additionally, a framework for automatically measuring LOF defect features, based on a U-net model combined with standard image processing techniques, is introduced. The results from these frameworks were utilized to conduct a detailed fatigue failure analysis of AM Ti-6Al-4V<sup>38</sup> specimens.

The specimens used in this study for fatigue life predictions were manufactured at various quality levels and subjected to heat treatment (HT) or HIP conditions. High-cycle fatigue tests were conducted until full fracture occurred. For each specimen, a comprehensive fractographic analysis was performed, and 14 features were measured using the proposed defect-measuring framework to fully characterize each initiation site. A dataset was generated from these mea-

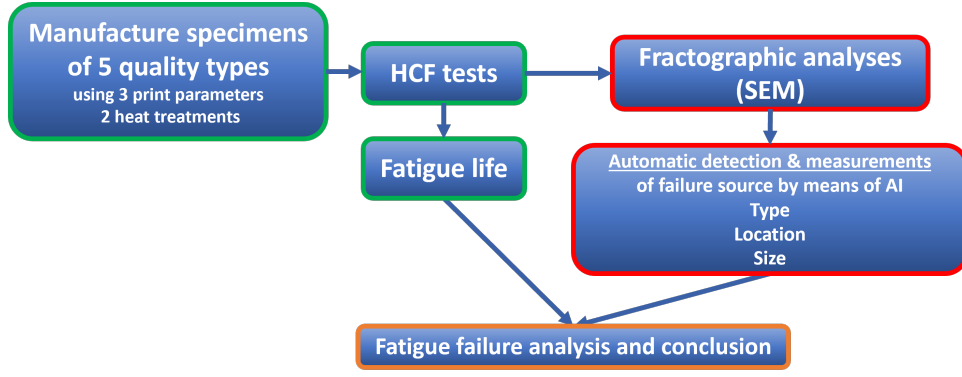


Figure 2: **Research methodology**

surements, and correlations with the measured fatigue life were established. From the analysis of these features, it was demonstrated that, for all printing qualities, the critical defect size and distance from the surface are bounded by specific dimensions. Feature importance was assessed, and the results were compared with key features identified in previous studies.

An innovative framework for the automatic failure analysis of additively manufactured Ti-6Al-4V specimens, based on defect characterization, is proposed. The framework examines the influence of various geometric and morphological defect characteristics obtained from destructive HCF tests across different specimen qualities. This approach has the potential to significantly expedite the failure analysis process while providing valuable insights into critical defect characteristics.

The remainder of the paper is structured as follows: Section 2 describes the materials tested and the research methodology. Section 3 presents the computer vision framework for automatic AI-based failure analysis, including the required dataset, identification of the fatigue failure source, distance measurement framework, and segmentation framework for measuring 14 characterizing geometrical and morphological features of the fatigue source. Section 4 provides the results and discussion on the correlation between the measured CTF and the feature measurements. Finally, Section 5 summarizes the key findings and conclusions of this investigation.

## 2 MATERIALS AND METHODS

The research methodology is illustrated in Fig. 2. The initial stage, highlighted in green frames, was carried out in Ref.<sup>11</sup> and involved the manufacturing 80 AM Ti-6Al-4V fatigue specimens, out of which 33 specimens were used in this study. The specimens were produced using Selective Laser Melting (SLM)<sup>39</sup> on an ALM EOS M290 machine (Laser-Power=340 W, Print-Layer-Thickness=60  $\mu\text{m}$ ), with varying print parameters corresponding to three different quality levels. All levels included the recommended parameters defined by EOS, with minor modifications to create higher and lower quality specimens. The three parameter sets are: *P1* – default

Table 1: Summary of specimen counts by quality group, printing parameters, and post-processing method (HT or HIP).

Printing quality	Printing parameters	HIP	HT	Total
P1	Default	7	8	15
P2	x2 stripe width	5	6	11
P3	x2 stripes distance	7	0	7
<b>Total</b>	-	19	14	33

recommended parameters, *P2* – improved quality, with the stripe width increased to double the EOS recommendation, and *P3* – lower quality, with the stripe distance increased to double the EOS recommendation. For each set of specimens, half underwent HIP post-processing following the procedure in Ref.<sup>40</sup> while the other half were subjected to standard HT at 800°C for 2 hours in an Argon atmosphere (furnace cooled, using optimized temperature control in the inert gas chamber). This resulted in six different specimen quality types. However, the P3 HT specimens were excluded from the study due to an excessive number of pores, making them unrepresentative for analysis. Table 1 summarizes the number of specimens for each printing group across four columns: quality group, modified printing parameters, number of specimens with HT treatment, and those with HIP treatment. The final row and column present the total specimen count.

To eliminate surface roughness as a potential factor in fatigue crack initiation, all specimen surfaces were machined to a surface roughness quality of N6 (32  $\mu\text{in}$ ). The manufactured specimens were then subjected to HCF tests following<sup>41</sup> with a maximum stress of 634 MPa and a stress ratio of  $R_p = 0.1$ .

Following this, as indicated by the red frames in Fig. 2, a fractographic analysis was performed. The initiation sites were categorized, and features such as distance to the surface and defect area were measured manually. Subsequently, the method described in Ref.<sup>37</sup> was utilized along with several enhancements as will be described in Section 3.2. In addition, a computer vision-based framework was developed to measure the geometrical and morphological features of the fatigue source automatically as will be described in Section 3.

In the final stage, highlighted by the orange frames in Fig. 2, a failure analysis was conducted using the generated data to identify patterns and correlate the measured CTF with various measured features. This analysis also aimed to establish the bounding dimensions and significance of each feature in contributing to premature failure. Finally, the *X*-parameter model was employed and examined with the scattered data. The proposed framework can facilitate automatic post-failure inspections and aid in determining specific mechanical and geometrical characteristics of critical defects in the future.



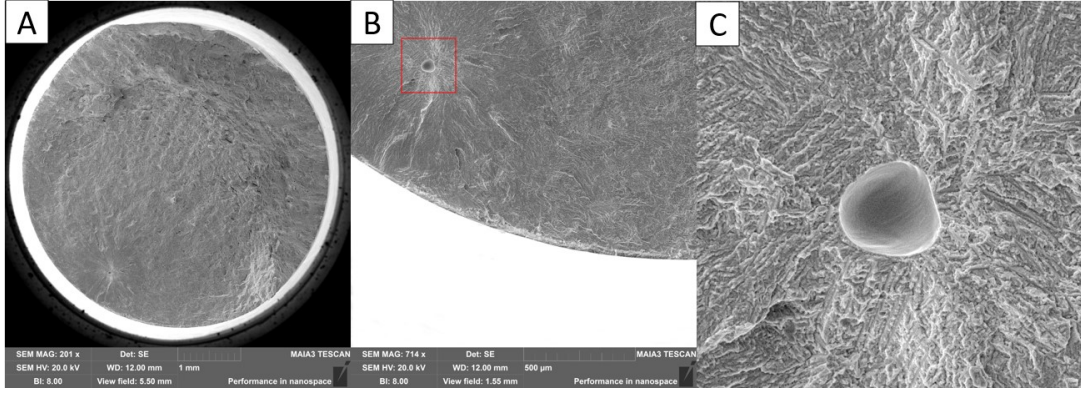


Figure 3: **SEM scans of the fractured surface: (A) The entire fractured surface (pixel size of  $1.34 \mu\text{m}$ ), (B) The initiation site (pixel size of  $0.378 \mu\text{m}$ ), with the red box indicating the cropped area for image C, (C) A  $640 \times 640$  section of the LOF defect cropped from image B.**

### 3 Failure analysis automation framework

The following sections provide a detailed explanation of the framework utilized in this study to analyze and process the SEM images of fractured surfaces, focusing on defect identification, segmentation, and measurement. In Section 3.1, the datasets used are presented. The frameworks for measuring distances and segmenting defects from the images are described in Section 3.2 and Section 3.3. These methods are crucial for extracting meaningful information about the defects and automating the analysis.

#### 3.1 Dataset

In order to create the dataset used in this study, SEM images of the fractured surfaces were captured at two different resolutions, as shown in Fig.3A and 3B. The first image is a SEM scan of the entire fractured surface with a pixel size of  $1.34 \mu\text{m}$  and view field of 5.5 mm, as depicted in Fig.3A. This image type was utilized to identify the critical defect and measure the distance between its center and the specimen's outer surface, as described in Ref.,<sup>37</sup> with several enhancements introduced in this study. The second image, capturing the initiation site at a higher resolution with a pixel size of  $0.378 \mu\text{m}$  and a field of view of 1.55 mm, is shown in Fig.3B. Note that higher-resolution images are necessary to perform precise measurements of the defects. After scanning the specimen, regions where LOF defects were identified were manually cropped from the higher-resolution image using a  $640 \times 640$  pixel mask. An example of such an image is shown in Fig.3C. The mask size was selected to be sufficiently large with respect to the maximum LOF defect found.

Segmentation of high-resolution images was necessary to measure the geometric and morphological features of identified lack-of-fusion (LOF) defects. For defect segmentation, 44 defects

observed in high-resolution images from 11 tested specimens were analyzed. It is important to note that the dataset included both initiation sources and defects identified on the fractured surface that were not the primary cause of failure. Since random type initiation sites do not have a clear morphology or size, they were not suitable for this dataset, resulting in only 11 specimens being used. The final dataset used for defect segmentation comprised 56 cropped sections of  $640 \times 640$  pixels containing defects. Note that for some defects, multiple images were used. This occurred due to the scanning method for higher resolution images, where the fractured surface was divided into 16 overlapping sections, causing defects to sometimes appear in the overlap. However, due to slight variations in contrast and brightness, both instances of the defect differed and were therefore included in the dataset. Label annotations of the defects were created using the open-source tool VGG Image Annotator (VIA).

The dataset was partitioned into two subsets: a train set and a test set, with an 80-20 distribution ratio, respectively. Due to the small size of the training set, data augmentation was performed to increase its size artificially. Each image in the training set was rotated by a random selection of 2 out of 3 possible rotations ( $90^\circ$ ,  $180^\circ$ , and  $270^\circ$  degrees), effectively tripling the training set size. This approach aimed to enhance data variability and reduce the likelihood of over-fitting while artificially expanding the dataset for the defect segmentation framework.

### 3.2 Distance measurements

In this study, modifications to the framework suggested in Ref.<sup>37</sup> were made. For completeness, a short description of the framework in Ref.<sup>37</sup> is given here. The framework for detecting the fatigue crack initiation site comprised two deep learning models: a ResNet152 model used to filter out sections of the image that do not contain the initiation site and a YOLOv5 model trained to detect the initiation site in the remaining sections. Following the detection of the initiation site, a framework for measuring the distance to the surface was employed. This framework utilized standard image processing techniques such as Canny edge detection. It identified the center of the specimen, masked the specimen area, and, using this information, computed the distance to the surface.

The main modification to the framework developed in Ref.<sup>37</sup> is the replacement of the masking of the fractured surface via standard image processing techniques with a VGG16-based U-net. The U-net was trained to segment the fractured surface of the specimen, allowing for more precise detection of its outer contour. This, in turn, enabled a more accurate computation of the distance from the initiation site to the specimen's surface. Another modification involved applying a modified histogram equalization method to the SEM images, followed by retraining

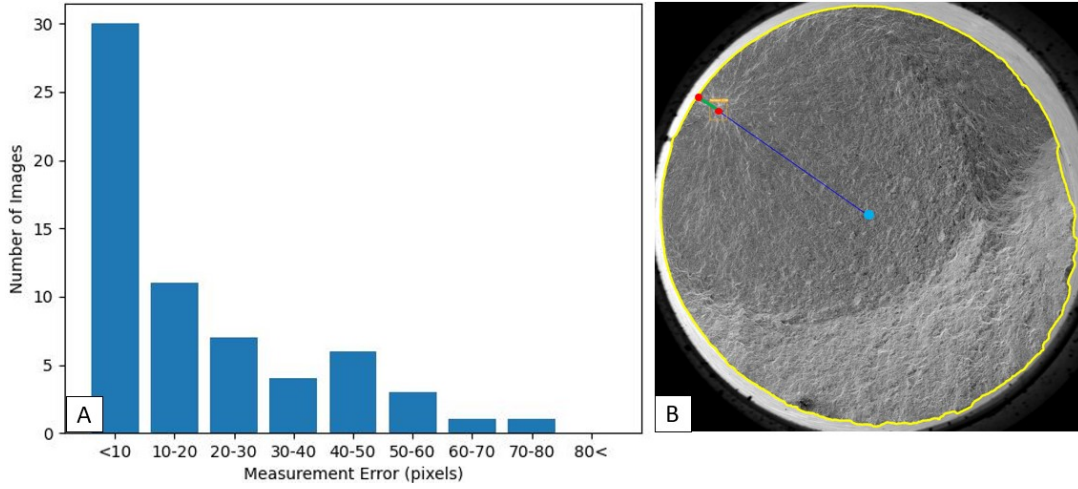


Figure 4: (A) Difference in pixels between the manual and autonomous measurements of the distance between the anomalies and the outer rim of the specimen. The anomaly was detected in 63 out of 65 images of the entire fractured surface. (B) An example of the distance measured is indicated by the green line.

the initiation site detection framework.

In Ref.<sup>37</sup> the same 33 specimens used in this study were examined. Note that each fractured specimen has two fractured surfaces, resulting in a total of 66 images. However, one fractured surface was damaged, leaving 65 images available for analysis. The initiation site was successfully detected in 61 out of these 65 images in Ref.<sup>37</sup> Whereas, in this study, the initiation site was detected in 63 out of 65 images.

The improved distribution of absolute errors in measuring the distance to the surface is illustrated in Fig.4A. The measured distance is shown by the green line in Fig.4B, where the two red dots indicate the center of the anomaly and the intersection point with the outer rim of the specimen. The average difference between the manual and autonomous measurements achieved in this study was 19 pixels, with a standard deviation (SD) of 19 pixels calculated as

$$SD = \sqrt{\frac{1}{N} \sum_{i=1}^N (x_i - \mu)^2} \quad (5)$$

where  $N = 63$  is the sample size,  $x_i$  is the absolute value of the individual difference between the distance measured automatically using the calculation model and measured manually for specimen  $i$ , and  $\mu$  is the mean value of  $x_i$  across all  $N$  specimens. Note that the manually measured values ranged between 6 pixels and 810 pixels. This error equates to an average difference of  $25.5 \mu\text{m}$ , representing a significant improvement from the average difference obtained in Ref.<sup>37</sup> of  $74.7 \mu\text{m}$ . These results translate to an average relative difference of 14.3%, with a SD of 14.1% calculated with  $x_i$  in eq. (5) as the individual relative difference between the automatically and the manually measured distance for specimen  $i$ .

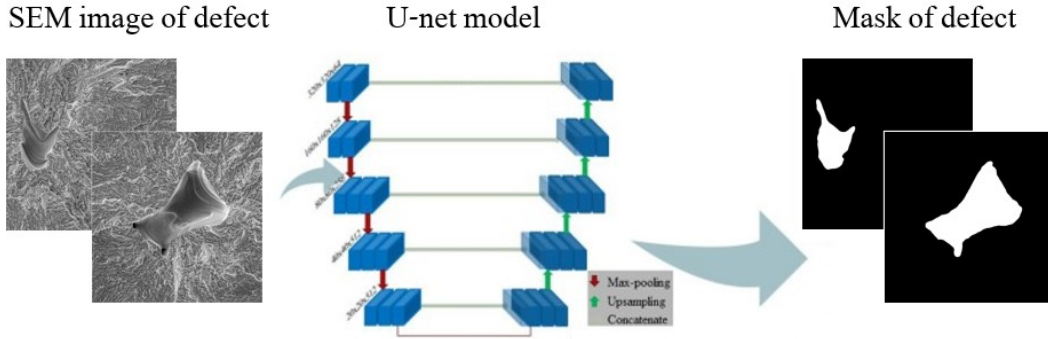


Figure 5: An illustration of the VGG16-based U-net model used to Segment LOF defects from SEM images.

### 3.3 Segmentation framework

A supplementary VGG16-based U-net model was specifically trained to segment LOF defects from the higher-resolution images of the initiation site, as detailed in Section 3.1. An illustration of the model is shown in Fig. 5, where the input to the U-net model consists of SEM images with LOF defects, and the output is the predicted masks of the defects. The training set initially consisted of 45 images prior to augmentation, while the test set included 11 images. During training, a batch size of 4 was utilized, and the model underwent training for 100 epochs, with the best-performing weights being saved. The evaluation of the training process involved assessing the performance of the model using the average IoU, calculated according to

$$IoU(Prediction, Label) = \frac{Prediction \cap Label}{Prediction \cup Label}, \quad (6)$$

on the test set.

Following model training, standard image processing techniques were applied to the model's predictions to extract 14 features which are detailed in Table 2. To reduce noise from model predictions where the model incorrectly segments additional small pixel groupings as defects, the algorithm assumes that the image contains only a single LOF defect. Consequently, only the largest contour in terms of area within the prediction is analyzed. This assumption is valid, as the segmentation model is part of a larger framework. Based on the model developed by<sup>37</sup> to detect LOF defects in the lower resolution images of the entire fractured surface, a  $640 \times 640$  image of the identified defect, with pixel size of  $0.378 \mu\text{m}$ , can be captured autonomously by the SEM.

## 4 RESULTS

In this section, the results achieved in this study are described. Section 4.1 discusses the influence of printing quality and heat treatment on fatigue life. In Section 4.2, the improved

Table 2: **Parameters derived from defect masks that are employed in the machine learning analysis. Measurements are initially calculated in pixel values and subsequently converted to units of micrometers ( $\mu m$ ).**

Parameter	Symbol	Units	Description
Area	S	$\mu m^2$	Area of defect
Perimeter	C	$\mu m$	Perimeter length of defect
Major axis length	a	$\mu m$	Major axis length of ellipse approximation for the defect
Minor axis length	b	$\mu m$	Minor axis length of ellipse approximation for the defect
Eccentricity	e	-	Eccentricity of approximation ellipse: $\frac{\sqrt{a^2-b^2}}{a}$
Convex Area	$S_c$	$\mu m^2$	Area of defect convex
Bounding box area	$S_b$	$\mu m^2$	Area of defect bounding box
Equivalent diameter	$D_e$	$\mu m$	Diameter of circle with equivalent area to defect: $\sqrt{\frac{4S}{\pi}}$
Max Feret diameter	$D_{f_{max}}$	$\mu m$	Max Feret diameter of defect
Min Feret diameter	$D_{f_{min}}$	$\mu m$	Min Feret diameter of defect
Circularity	-	-	Resemblance of defect shape to a circle: $4\pi \cdot \frac{S}{C^2}$
Solidity	-	-	Area to convex area ratio: $\frac{S}{S_c}$
Extent	-	-	Area to bounding box area ratio: $\frac{S}{S_b}$
Angularity	-	-	Resemblance between defect and approximated ellipse: $\frac{ 4S-a \cdot b \cdot \pi }{4S}$

results for the distance-to-surface measuring framework are presented. Finally, Section 4.3 details the results of the defect segmentation and measurement framework. For this analysis, three specimens were excluded, resulting in the evaluation of only 30 specimens. Two of the excluded specimens exhibited unique defects not found in the rest of the dataset: one had a large LOF surface, and the other had a surface defect. Additionally, another specimen was excluded due to being an outlier in terms of fatigue life. It is worth noting that both the specimen with the large LOF surface and the outlier regarding fatigue life were produced using the lowest print quality P3.

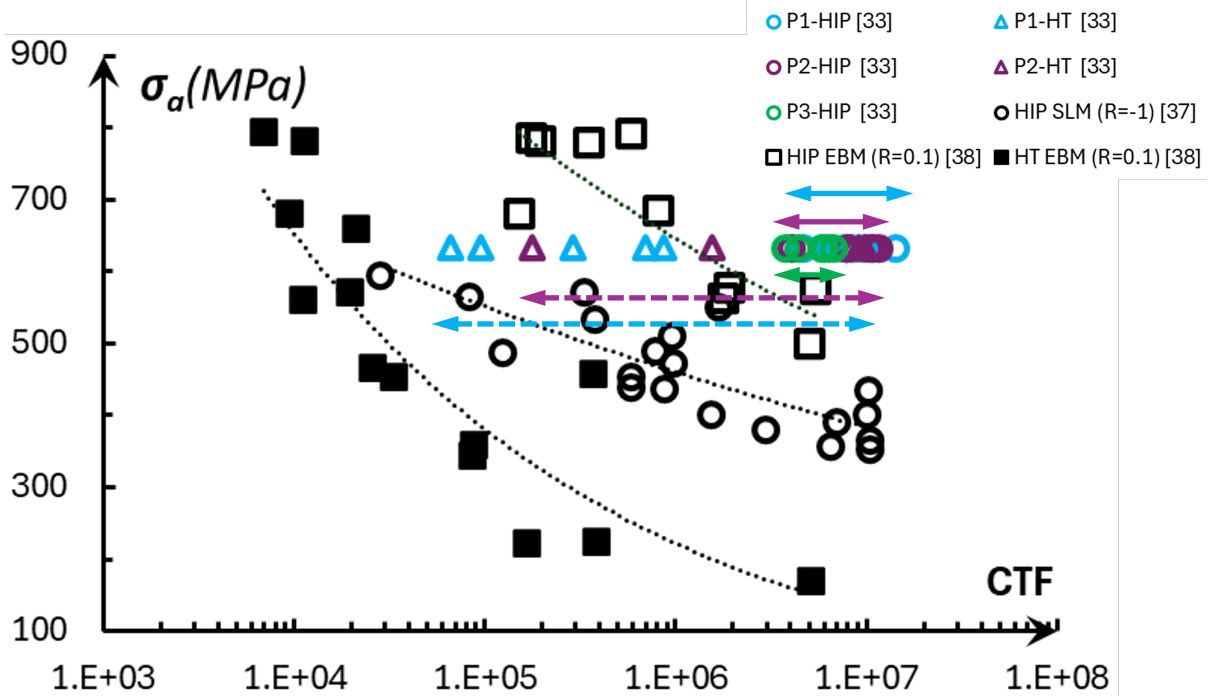


Figure 6: S-N curves illustrating the relationship between maximum applied stress and cycles to failure (CTF) for the specimens examined in this study, of which were tested in study Ref.<sup>11</sup> The results are compared with data from HIP-treated SLM AM Ti-6Al-4V specimens tested under  $R_P = -1$  from Ref.<sup>13</sup> as well as data from HIP-treated and heat-treated (HT) EBM AM Ti-6Al-4V specimens tested under  $R_P = 0.1$  from Ref.<sup>14</sup>

#### 4.1 Cycles to Failure Based on Printing Quality and Heat Treatment

In this section, a comparison of the CTF values across different printing qualities and post-processes is discussed. Figure 6 presents the resulting CTF values of the specimens examined in this study and compares them to the values obtained from HIP SLM Ti-6Al-4V specimens tested in  $R_P = -1$  in Ref.<sup>13</sup> and to the values obtained from HIP and HT EBM Ti-6Al-4V specimens tested in  $R_P = 0.1$  in Ref.<sup>14</sup> With the exception of several P1 HT specimens, the results for all printing qualities and post-processes in this study show higher CTF values than those reported in Ref.<sup>13</sup> and are within the bounded EBM results from Ref.<sup>14</sup> The scatter in the results is also evident in the figure, particularly for HT-treated specimens, which are marked with triangles. However, it is apparent that the scatter is substantially reduced for the HIP-treated specimens, which are marked with green, purple, and blue circles. Note that in Ref.<sup>11</sup> five additional specimens from the P3-HIP batch were tested and failed after a lower fatigue life. For these specimens, the fractographic analysis revealed high porosity, as demonstrated in Figure 7, and the fatigue source could not be determined. These specimens contributed to significant scatter in the P3-HIP data as reported in Ref.<sup>11</sup> The reduced scatter obtained here is a result of the omission of these specimens which were not used for the fractographic analysis performed here.



Figure 7: An example of a SEM image of one of the specimens from batch P3 which was dismissed from the analyses of this study due to high porosity which resulted in relatively low fatigue life.

To evaluate the effect of printing quality and heat treatment on fatigue life, Figs. 8a and 8b present the results for HIP and HT treatments, respectively, across the three printing qualities. Specimens are grouped into three CTF ranges:  $0 \leq \text{CTF} \leq 3.5$ ,  $3.5 < \text{CTF} \leq 8$ , and  $\text{CTF} > 8$ . The results show that for recommended and improved printing qualities, P1 and P2, respectively, characterized by fewer pores and LOF defects, HIP treatment was highly effective, with no specimens failing below 3.5 million cycles. In contrast, HT treatment, yielded poorer results for baseline P1 specimens, with five failing under 3.5 million cycles. Among the modified quality (P2) specimens treated with HT, three showed excellent fatigue lives exceeding 8 million cycles, while two failed below 3.5 million cycles. For P3 specimens, which exhibited numerous LOF defects, only HIP treatment was applied. While HIP offered a marginal improvement, the overall fatigue life of these specimens remained relatively low.

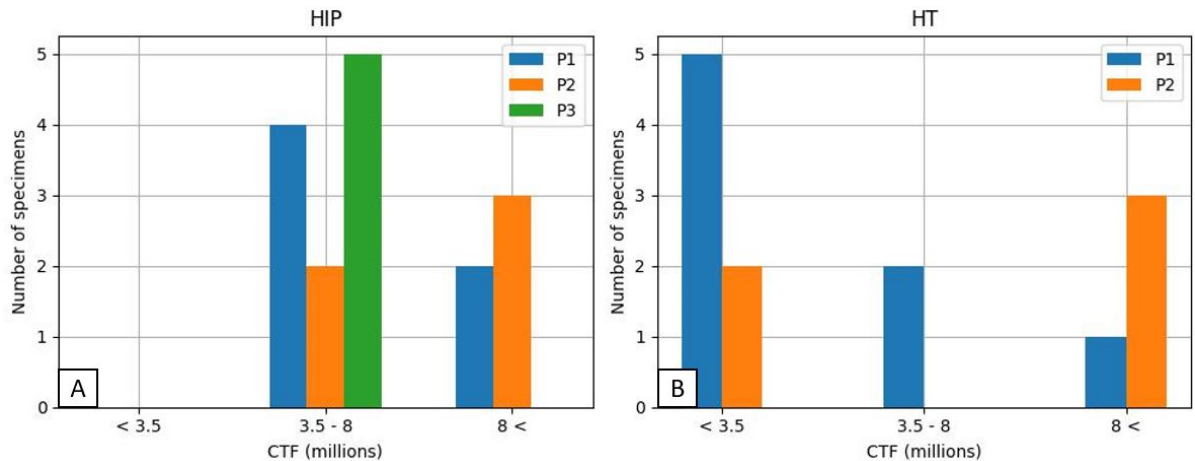


Figure 8: Number of specimens within various CTF ranges, categorized by printing quality and post-processing treatment. Panel (A) shows HIP specimens, (B) shows HT specimens.



Table 3: Median, mean and SD of CTF values for each printing quality and post-processing combination.

Printing Quality	Post-process	Median CTF	Mean CTF	SD	LOF	Random
P1	HIP	7,759,547	8,360,430	2,729,929	0	7
	HT	778,143	2,962,016	3,720,664	7	1
P2	HIP	10,399,595	8,908,806	2,735,179	0	5
	HT	8,268,660	5,761,666	4,052,435	3	2
P3	HIP	5,759,186	5,331,642	1,102,028	0	5
<b>Total</b>	HIP	-	-	-	0	17
	HT	-	-	-	10	3

In Table 3, the median and mean CTF values are summarized for each group. Both the improved P2 and baseline P1 HIP-treated specimens had mean CTF values exceeding 8 million cycles. However, for the specimens subjected to HT the CTF values reduced by 65% for P1 and 35% for P2. Interestingly, the median CTF for P1 was lower than the mean, whereas the opposite was true for P2, indicating skewness in the data. The high SD for P2 specimens further reflects this variability. For P3 specimens, the mean CTF was more normally distributed with a mean value of approximately 5.3 million cycles which is relatively low.

Also, in Table 3, the types of defects identified for each group are specified. Recall that LOF defects include both lack of fusion and pores. The table reveals that HIP-treated specimens generally have random-type failure sources, while HT-treated specimens retained more LOF defects with consistent morphology and size.

## 4.2 Distance measurements

The correlation between the measured distance and the CTF for the 30 tested specimens is shown in Fig. 9. The plot legend in the figure provides details on the post-processing method for each specimen (HT or HIP) and the type of killer defect identified. Notably, in the HIP-processed specimens (marked in red), only 'random' defects were identified, while in the HT-treated specimens, the majority (10 specimens, marked in blue) contained an LOF defect, with only 3 specimens (marked in yellow) showing a 'random' defect.

It may be observed from the figure that generally, initiation sites closer to the specimen surface correlate with shorter fatigue life. Particularly, specimens with an LOF defect with a fatigue life of less than 1.6 million cycles generally exhibited initiation sites located within a distance smaller than 0.025 mm to the surface. The single random specimen that resulted in a fatigue life shorter than 1.6 million cycles included a random fatigue source identified within 0.1 mm from the specimen surface. As for the other specimens with fatigue lives longer than 3.7 million cycles, the fatigue source was observed at a distance larger than 0.16 mm from



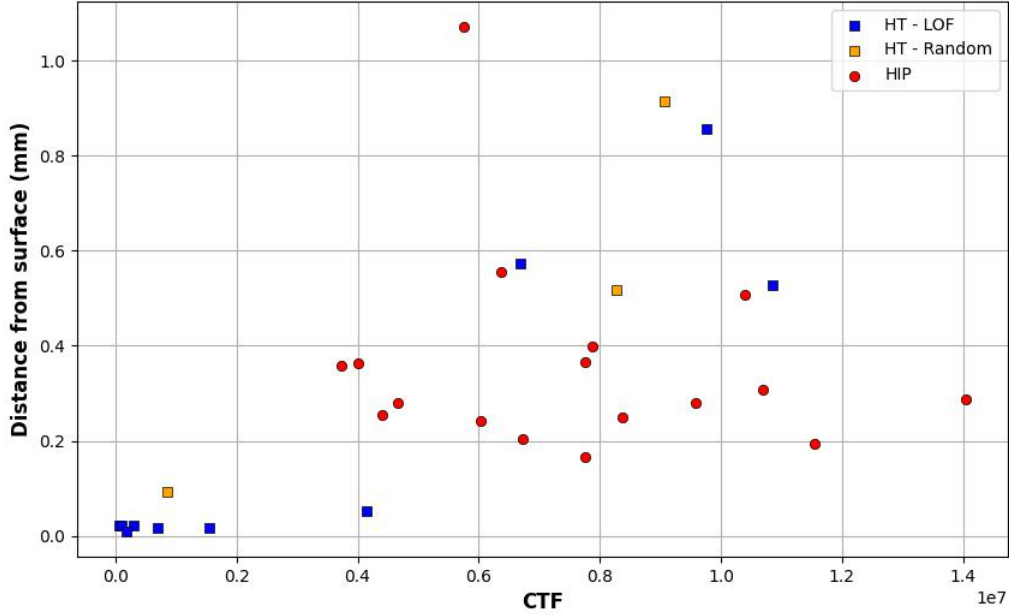


Figure 9: **Distance to the surface relative to CTF for all 30 specimens used in the ML analysis.**

the surface. Additionally, for HIP-treated specimens, initiation sites were typically located between 0.16 mm and 0.5 mm from the surface. In contrast, HT specimens exhibited a split pattern: some had initiation sites close to the surface with shorter fatigue lives, while others had initiation sites farther from the surface, corresponding to longer fatigue lives.

These results indicate that surface-adjacent defects, particularly LOF types, are critical contributors to reduced fatigue life. Hot isostatic pressing (HIP) post-processing is well-documented to enhance fatigue performance.<sup>13,14</sup> In this study, it was observed that "random" failure sources were displaced deeper into the material following HIP treatment, resulting in improved fatigue performance compared to HT processing. This finding highlights the importance of optimizing post-processing techniques and defect management strategies in AM.

### 4.3 Defect Segmentation

Following the training methodology detailed in Section 3.3, the highest mean IoU achieved for the test set was 0.836. It is noteworthy that when training was conducted without augmentation, the upper limit for the test IoU was approximately 0.78. The results for two images in the test set are illustrated in Fig.10. In Fig.10A, the model accurately predicted the defect, with negligible differences between the label and predictions. However, in Fig. 10B, although the IoU was 0.83, there is a noticeable difference primarily due to the model incorrectly predicting an additional part of the image belonging to the defect.

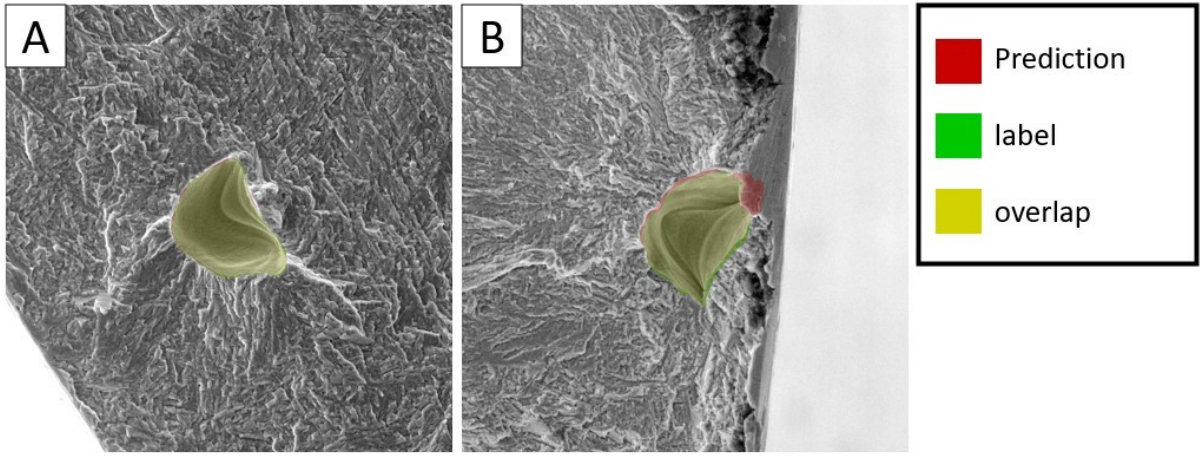


Figure 10: **Two images from the test set: (A) Image with an IoU of 0.95 and (B) Image with an IoU of 0.83. In both images, the yellow-tinted area represents the overlap between the prediction and the label. The green area is part of the label, but is not predicted by the model, while the red areas were predicted by the model to be part of the defect but are not.**

Since the goal of defect segmentation was to compute 14 features for subsequent failure analysis, the computed features for both the labels and predictions of the test set are compared in Table 4. Note that the SD values in columns four, six, and eight in Table 4 correspond to the feature value measured manually, the absolute error between the automatic and manual measurements of the feature, and the absolute relative error between the automatic and manual measurements, respectively. The SD was calculated for each case using eq. (5) with  $N = 11$ , where  $x_i$  refers to the manually measured value of specimen  $i$ , the absolute difference between the feature measured automatically and manually for specimen  $i$ , or the relative difference between the two measurements for specimen  $i$ , and  $\mu$  is the mean value of  $x_i$  across all  $N$  specimens. It may be observed from Table 4 that the measured dimensions shown in the third column for all features and the SDs for these measurements, given in the fourth column, are approximately the same. This indicates that the initiation site dimensions are distributed over a large range. Similarly, the accuracy of the U-net measurement compared with the labeled values is also distributed over a large range, as may be understood from the mean absolute error and mean relative error for these measurements given in the fifth and seventh columns, respectively, and the SDs of each error type in columns six and eight, which are also approximately the same size. For some features, namely 'minor axis length,' 'Max Feret diameter,' and 'Min Feret diameter,' it may be observed in Table 4 that the SD values related to the absolute error are larger than the mean. This is because, for these features, two or three specimens exhibited significantly larger errors between the automatic and manual measurements compared to the other specimens. These outliers skewed the data, leading to a substantial increase in the SD values. Note that the average relative error for most features is approximately 10%.

Table 4: Mean and SD of manually measured defect features, with absolute and relative errors between segmentation model predictions and ground truth measurements.

Parameter	Units	Measured Value		Absolute Error		Relative Error [%]	
		Mean	SD	Mean	SD	Mean	SD
Area	$\mu m^2$	2,432.8	1,874.6	149.3	112.0	9.9	10.2
Perimeter	$\mu m$	208.7	88.6	11.9	9.6	7.4	7.4
Major axis length	$\mu m$	68.9	26.8	4.1	3.5	7.5	7.9
Minor axis length	$\mu m$	45.7	19.5	2.9	3.7	6.9	7.0
Eccentricity	-	12.4	3.9	2.4	1.7	21.5	16.4
Convex Area	$\mu m^2$	2,808.8	2,455.5	141.0	132.9	10.0	10.1
Bounding box area	$\mu m^2$	4,613.5	4,686.5	220.7	167.5	10.5	10.0
Equivalent diameter	$\mu m$	51.8	20.4	2.0	1.5	4.9	5.0
Max Feret diameter	$\mu m$	75.4	24.6	7.4	14.4	10.0	17.8
Min Feret diameter	$\mu m$	47.2	18.2	5.1	5.6	13.6	16.9
Circularity	-	0.62	0.13	0.06	0.04	10.1	7.3
Solidity	-	0.89	0.07	0.03	0.02	3.2	3.0
Extent	-	0.57	0.11	0.04	0.03	7.5	5.5
Angularity	-	0.17	0.14	0.03	0.03	41.1	53.3

The correlation between the 14 manually measured features and the CTF for the 10 specimens with LOF initiation sites is illustrated in Figs. 11 through 13. The area-related features are shown in Fig. 11, while length- and ratio-related features appear in Fig. 12 and Fig. 13, respectively. As concluded in Fig. 9, initiation sites closer to the specimen surface are associated with shorter fatigue life. The data in Fig. 11 and Fig. 12 indicate that specimens with surface-adjacent initiation sites tend to have smaller defects, with area features below  $3000 \mu m^2$  and corresponding length features lower than those found in specimens with longer fatigue lives. It is worth noting that while all area-related features produced similar results and trends, the most pronounced differences were observed in the bounding box area feature. Although the threshold for length-related features varies, clear distinctions for fatigue life above or below 1.6 million cycles are evident for most features. For example, lower fatigue life specimens generally have a perimeter less than  $185 \mu m$ , an equivalent diameter smaller than  $42 \mu m$ , a major axis

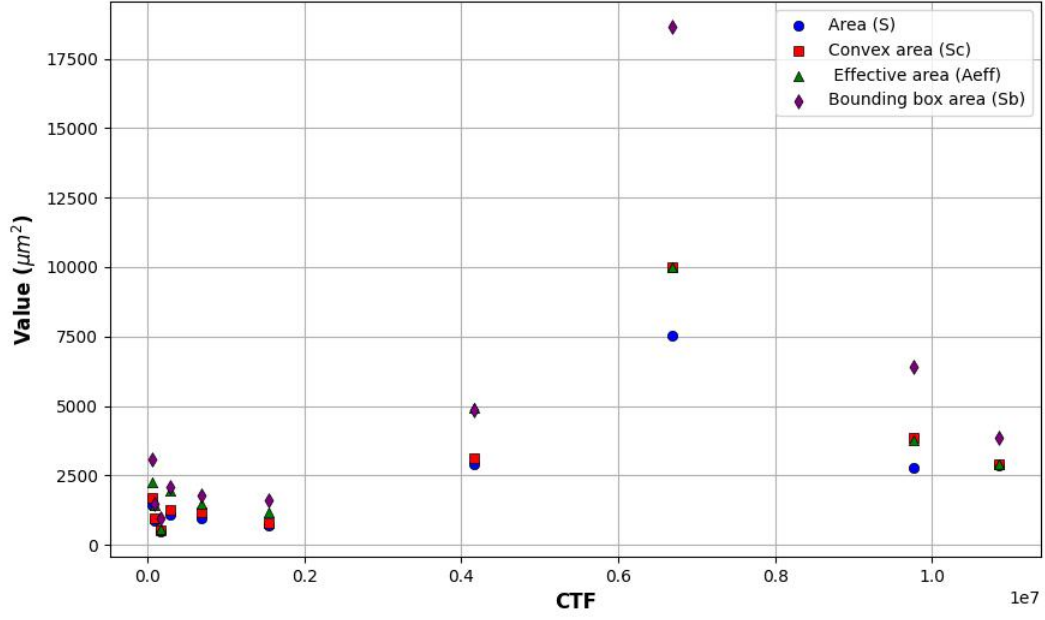


Figure 11: Area features for the 10 specimens with LOF initiation sites as a function of the CTF.

shorter than  $67\ \mu\text{m}$ , and a minor axis shorter than  $35\ \mu\text{m}$ . A noticeable borderline appears for most measured constants around the 1.6 million cycle mark.

In contrast, specimens with fatigue lives over 1.6 million cycles failed due to larger defects

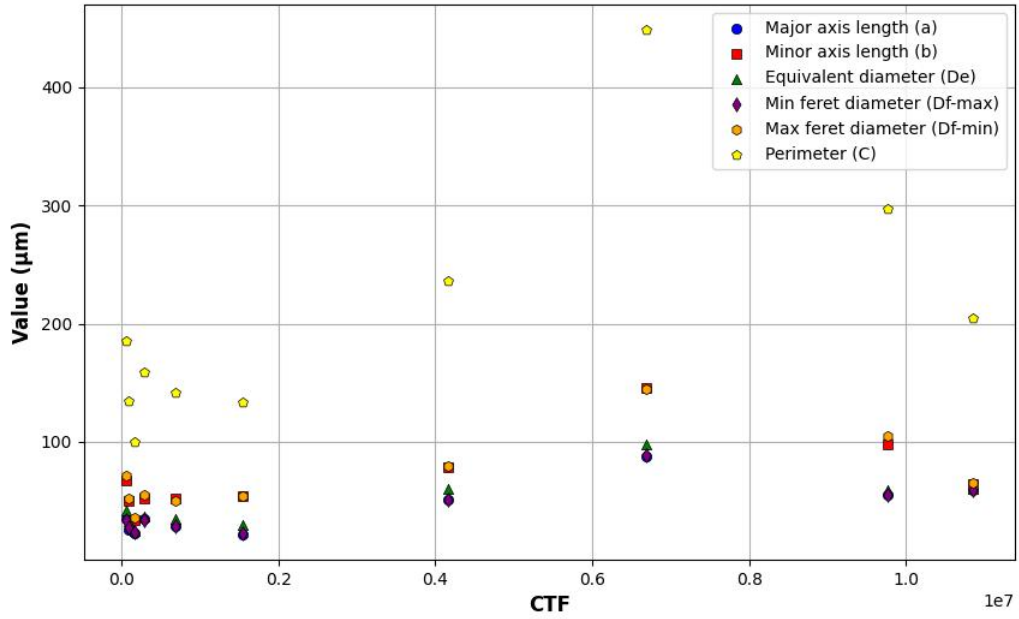


Figure 12: Length features for the 10 specimens with LOF initiation sites as a function of the CTF.

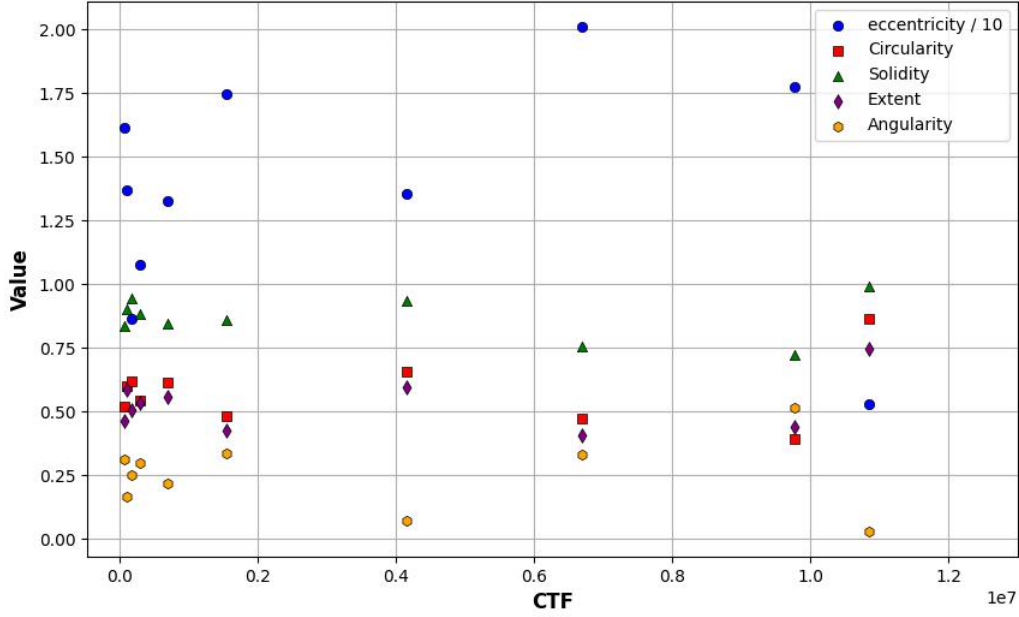


Figure 13: **Ratio features for the 10 specimens with LOF initiation sites as a function of the CTF.**

located farther from the surface. This suggests that defect size is critical for determining fatigue life, alongside the defect's distance from the surface. The absence of large killer defects near the surface and small defects farther from it minimizes the observable impact of area and length features on fatigue life, making them secondary factors related to defect criticality. Additionally, the lack of large defects near the surface could indicate that standard HT may partially seal surface-adjacent pores or that larger LOF defects tend not to form near the surface. Regarding ratio-related features, as depicted in Fig. 12, no clear correlation was evident between these features and fatigue life.

A plot of the distance from the surface versus the square root of the convex area,  $\sqrt{\text{area}}$ , for all LOF killer defects identified is presented in Fig. 14A, showing data for ten specimens. The figure demonstrates that as the distance from the surface decreases, smaller defects become critical. In Fig. 14B, only specimens with a distance smaller than 0.16 mm are included. A linear correlation between the two parameters is observed, given by

$$\text{Distance} = \sqrt{\text{area}} - 13.76 \quad . \quad (7)$$

This linear relationship may provide a means to determine critical small defects based on their distance from the surface.

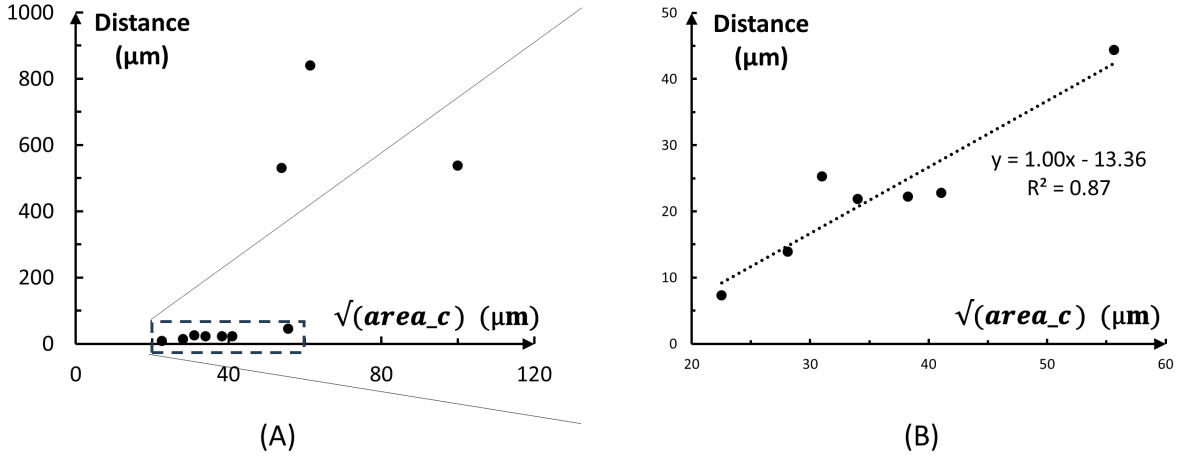


Figure 14: Defect distance from the surface versus  $\sqrt{\text{area}}$ : (A) Ten specimens with LOF killer defects identified. (B) Seven specimens from the ten shown in (A) with a defect distance from the surface smaller than 0.16 mm, revealing a linear correlation: as the distance from the surface increases, the  $\sqrt{\text{area}}$  also increases.

#### 4.4 Cycles to failure - prediction models

The geometrical and morphological characterizations measured in this study using the segmentation algorithm described in Section 3.3, and the results presented in Section 4.3, respectively, were used for the  $X$ -parameter model in eq. (4). This model enables the prediction of the CTF based on the features of distance from the surface ( $D$ ),  $\sqrt{\text{area}}$ , and circularity ( $C$ ) of the identified defect.

The  $X$ -parameter was calculated for the ten LOF killer defects identified. The model parameters  $\alpha$  and  $\beta$  were optimized using the least squares method with the Generalized Reduced Gradient (GRG) solver in Excel,<sup>42</sup> yielding values of  $\alpha = 0.45$  and  $\beta = 2.18$ .

The resulting curve, shown in Fig. 15, demonstrates a clear inverse correlation: as the  $X$ -parameter increases, CTF decreases. This reflects the combined effect of defect size, proximity to the surface, and morphology. Larger or surface-near defects cause higher stress concentrations, which accelerate crack initiation and material failure.

This strong correlation, with an  $R^2$  value of 0.91, validates the  $X$ -parameter model's accuracy in predicting  $N_f$  and highlights its capability to integrate the combined effects of defect size, location, and morphology. The resulting criterion may be applied to predict fatigue life in specimens with LOF defects. These findings underscore the robustness of the  $X$ -parameter model as a versatile tool for predicting fatigue life and optimizing defect tolerances in industrial components across various manufacturing methods.

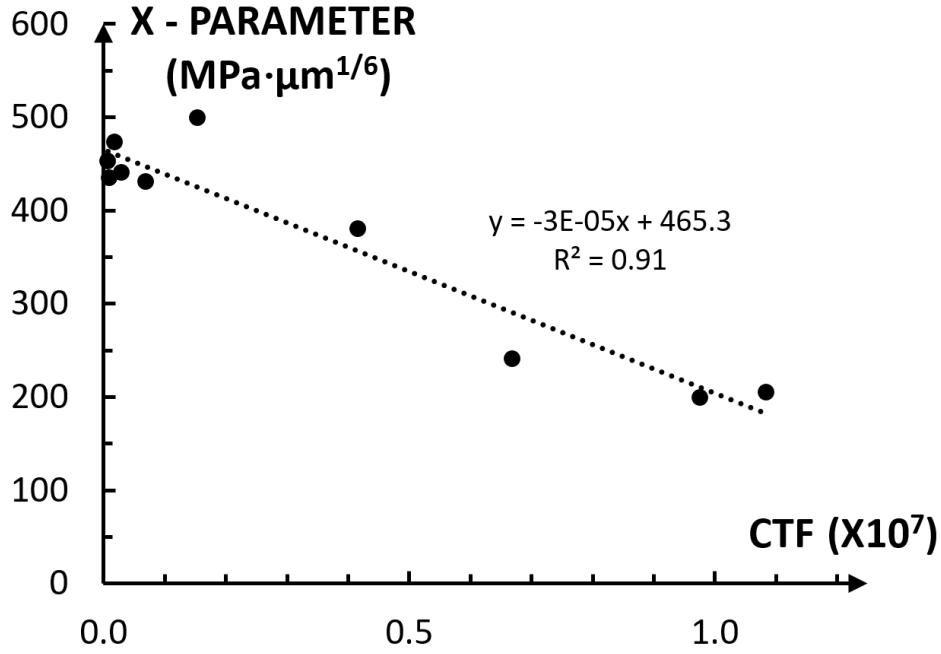


Figure 15: The X-parameter from eq. (4) for the 10 specimens with identified LOF fatigue sources, plotted against the CTF measured in the tests. The dotted line represents the linear fit to the data, with  $\alpha = 0.45$ ,  $\beta = 2.18$ , and  $R^2 = 0.91$ .

## 5 DISCUSSION AND CONCLUSIONS

In this study, AM Ti-6Al-4V specimens, produced via SLM at three quality levels and subjected to either HIP or HT post-processing, were tested for fatigue. After testing, each fractured surface was scanned using SEM for failure analysis to identify "killer" defects and provide geometrical and morphological characterization. Of the 33 specimens tested, 30 were included in the analysis. Among these, 10 contained visible LOF defects, while the remaining specimens showed failure initiated by random defects. The HIP-treated specimens exhibited reduced scatter in fatigue life and a higher average fatigue life across all quality levels.

To automate the identification of failure sources and measure the distance between the defect center and the specimen surface, a model adapted from<sup>37</sup> was modified and used. For LOF defects, a VGG16-based U-net and image processing framework was employed to extract 14 key geometrical and morphological features (see Table 2). To mitigate errors caused by SEM specimen tilt, values for these 14 features along with the distance to the surface were averaged across two fractured surface measurements for each specimen.

Upon analysis of the results, the following conclusions can be drawn:

- A U-net model successfully enhanced the algorithm for measuring the distance to the fatigue crack initiation site by improving the detection of the specimen's outer contour. The average measurement error decreased from 55.6 pixels in Ref.<sup>37</sup> to 19 pixels, reducing

the average error from 74.7  $\mu\text{m}$  to 25.5  $\mu\text{m}$ .

- Defect segmentation with augmentation achieved an average test IoU of 0.836, showing that a VGG16-based U-net can yield good results even with a relatively small training dataset, making it a valuable tool for automating fractographic analyses.
- Three printing levels, combined with HIP or HT post-processing, were examined. The average fatigue life was well correlated with the respective printing levels.
- Correlation between heat treatment and the measured CTF, as shown in Fig. 6 and Table 3, revealed that HIP substantially improved the fatigue performance of all AM SLM specimens tested. This result aligns with previous studies.<sup>9,11,13,14</sup>
- The most significant factor influencing failure was the distance from the surface, supporting previous findings that proximity to the surface is linked to premature failure.<sup>5,11</sup> Particularly, specimens with an LOF defect with a fatigue life of less than 1.6 million cycles generally exhibited initiation sites located within a distance smaller than 0.025 mm to the surface.
- HIP-treated specimens exhibited mostly random initiation sites. These sites were located within a band approximately 0.16  $\mu\text{m}$  through 0.5  $\mu\text{m}$  from the surface.
- A correlation between defect size and distance to the surface was observed. When defects are located within 0.025 mm of the surface, smaller defects are more detrimental to fatigue life. Beyond this distance, defect size showed larger influence on fatigue life, suggesting that the impact of defect size increases as the distance from the surface increases.
- Defects with area features smaller than 3000  $\mu\text{m}^2$  were associated with shorter fatigue lives. The most pronounced differences in area features were observed for the Bounding box area.
- For specimens with fatigue lives below 1.6 million cycles, a trend emerged where smaller defects resulted in longer fatigue lives. Additional testing could confirm this trend through curve fitting with a possible saturation limit.
- No conclusive trend was found regarding defect morphology (e.g., angularity or circularity), indicating these characteristics do not play a deterministic role in failure.
- The  $X$ -parameter model demonstrated a clear trend and can be used as a fatigue life prediction model that correlates defect location, size, and morphology. The  $R^2$  value of the  $X$ -parameter model was found to be 0.91, with  $\alpha = 0.45$  and  $\beta = 0.18$ . These



parameters were optimized to relate two distinct printing qualities, P1 and P2, of Ti-6Al-4V specimens tested under HCF conditions.

The main limitation of this study was the small dataset size. Expanding the dataset by including more specimens is essential to gain deeper insights from the analysis. A larger dataset could enhance the accuracy of the LOF measurement framework. Additionally, incorporating further data augmentation techniques, such as brightness and contrast adjustments, could improve the model's performance, complementing the rotation-based augmentation already in use.

The proposed automated fractographic defect detection and measurement framework could be a valuable tool for streamlining the fractographic analysis process, enabling the generation of reliable, quantitative results and trends related to defect location, morphology, and size. With more data, advanced hybrid machine learning techniques that may account for physical or phenomenological models such as the  $X$ -parameter model could be applied, uncovering stronger correlations between defect features and fatigue life.

Improving the accuracy and robustness of automatic failure analysis could drive the practical adoption of AM materials in various industries. Furthermore, the findings from this study offer valuable insights into the fatigue failure of AM materials.

## ACKNOWLEDGEMENTS

The authors would like to express their deepest gratitude to the Electron Microscopy Unit (Technology and Engineering department) at Ariel University for its crucial role in supporting this research. Special thanks go to Dr. Olga Krichevsky and Dr. Tamara Brider for their patience and unwavering availability to assist students at all times, as well as for their expertise in conducting the SEM scans used in this study.

The authors also wish to thank Prof. Shmuel Osovski for his valuable recommendations throughout the research process. Finally, the authors extend their appreciation to Israel Aerospace Industries (IAI), particularly Ms. Yael Motola, for their support of this research.

## AUTHOR CONTRIBUTIONS

**Ro'i Lang:** Conceptualization; project administration; methodology; investigation; writing original draft; writing review editing. **Or Haim Anidjar:** Supervision; methodology; writing review editing; **Sahar Slonimsky:** Formal analysis; **Chen Hajaj:** Supervision; investigation; writing review editing; **Oz Golan:** Materials preparation; **Carmel Matias:** Conceptualization; writing review editing; **Alex Diskin:** Conceptualization; **Strokin Evgeny:** Specimen

manufacturing; HCF tests; **Mor Mega:** Supervision; project administration; conceptualization; methodology; investigation; resources; writing original draft; writing review editing;

## **DATA AVAILABILITY STATEMENT**

Data will be made available upon request.

## References

- [1] Sing SL, An J, Yeong WY, Wiria FE. Laser and electron-beam powder-bed additive manufacturing of metallic implants: A review on processes, materials and designs. *Journal of Orthopaedic Research* 2016;34:369–385.
- [2] Uriondo A, Esperon-Miguez M, Perinpanayagam S. The present and future of additive manufacturing in the aerospace sector: A review of important aspects. *Proceedings of the Institution of Mechanical Engineers, Part G: Journal of Aerospace Engineering* 2015;229:2132–2147.
- [3] Blakey-Milner B, Gradl P, Snedden G, Brooks M, Pitot J, Lopez E, Leary M, Berto F, du Plessis A. Metal additive manufacturing in aerospace: A review. *Materials & Design* 2021;209:110008.
- [4] Edwards P, Ramulu M. Fatigue performance evaluation of selective laser melted Ti-6Al-4V. *Materials Science and Engineering: A* 2014;598:327–337.
- [5] Leuders S, Thöne M, Riemer A, Niendorf T, Tröster T, Richard Ha, Maier H. On the mechanical behaviour of titanium alloy TiAl6V4 manufactured by selective laser melting: Fatigue resistance and crack growth performance. *International Journal of Fatigue* 2013;48:300–307.
- [6] Loh N, Sia K. An overview of hot isostatic pressing. *Journal of Materials Processing Technology* 1992;30:45–65.
- [7] Qiu C, Adkins NJ, Attallah MM. Microstructure and tensile properties of selectively laser-melted and of HIPed laser-melted Ti-6Al-4V. *Materials Science and Engineering: A* 2013;578:230–239.
- [8] Tong Z, Ren X, Jiao J, Zhou W, Ren Y, Ye Y, Larson EA, Gu J. Laser additive manufacturing of FeCrCoMnNi high-entropy alloy: Effect of heat treatment on microstructure, residual stress and mechanical property. *Journal of Alloys and Compounds* 2019;785:1144–1159.
- [9] Fatemi A, Molaei R, Sharifimehr S, Phan N, Shamsaei N. Multiaxial fatigue behavior of wrought and additive manufactured Ti-6Al-4V including surface finish effect. *International Journal of Fatigue* 2017;100:347–366.
- [10] Malekipour E, El-Mounayri H. Common defects and contributing parameters in powder bed fusion AM process and their classification for online monitoring and control: A review. *The International Journal of Advanced Manufacturing Technology* 2018;95:527–550.
- [11] Matias C, Diskin A, Golan O, Garkun A, Storkin E. Ti-6Al-4V additive manufacturing measure of quality according to fatigue crack initiation vs. crack propagation. In: *Icas - international council of the aeronautical sciences. ICAS, 2022* [https://www.icas.org/ICAS\\_ARCHIVE/ICAS2022/data/papers/ICAS2022\\_0036\\_paper.pdf](https://www.icas.org/ICAS_ARCHIVE/ICAS2022/data/papers/ICAS2022_0036_paper.pdf).
- [12] Chakotay E, Shneck RZ, Golan O, Carmi R, Mega M, Alon I, Yakov R, Busiba A. Effects of anisotropic microstructure and load ratio on fatigue crack propagation rate in additively manufactured ti-6al-4v alloy. *Metals* 2024;14:1405.
- [13] Mertova K, Dzugan J, Roudnicka M. Fatigue properties of SLM-produced Ti6Al4V with various post-processing processes. In: *Iop conference series: materials science and engineering*. IOP Publishing, Volume 461, 2018 p 012052.
- [14] Hrabe N, Gnäupel-Herold T, Quinn T. Fatigue properties of a titanium alloy (Ti-6Al-4V) fabricated via electron beam melting (EBM): Effects of internal defects and residual stress. *International Journal of Fatigue* 2017;94:202–210.

- [15] Sanaei N, Fatemi A. Defects in additive manufactured metals and their effect on fatigue performance: A state-of-the-art review. *Progress in Materials Science* 2021;117:100724.
- [16] Mohammed A, Abdullah A. Scanning electron microscopy (SEM): A review. In: *Proceedings of the 2018 international conference on hydraulics and pneumatics—hervex, băile govora, romania. INOE 2000-IHP, 2018* <https://fluidas.ro/hervex/proceedings2018/77-85.pdf>.
- [17] Junet A, Messenger A, Weck A, Nadot Y, Boulnat X, Buffiere JY. Internal fatigue crack propagation in a Ti-6Al-4V alloy: An in situ study. *International Journal of Fatigue* 2023;168:107450.
- [18] Rohrer GS. Grain boundary energy anisotropy: A review. *Journal of materials science* 2011;46:5881–5895.
- [19] Murakami Y. Metal fatigue: effects of small defects and nonmetallic inclusions. Academic Press, 2019.
- [20] Murakami Y, Endo M. Prediction model of sn curve without fatigue test or with a minimum number of fatigue tests. *Engineering Failure Analysis* 2023;154:107647.
- [21] Masuo H, Tanaka Y, Morokoshi S, Yagura H, Uchida T, Yamamoto Y, Murakami Y. Effects of defects, surface roughness and HIP on fatigue strength of Ti-6Al-4V manufactured by additive manufacturing. *Procedia Structural Integrity* 2017;7:19–26.
- [22] Zhu ML, Jin L, Xuan FZ. Fatigue life and mechanistic modeling of interior micro-defect induced cracking in high cycle and very high cycle regimes. *Acta Materialia* 2018;157:259–275.
- [23] Hu Y, Wu S, Xie C, Wu W, Zhang J. Fatigue life evaluation of Ti-6Al-4V welded joints manufactured by electron beam melting. *Fatigue Fract Eng Mater Struct* 2021;44:2210–2221.
- [24] Boateng EY, Otoo J, Abaye DA. Basic tenets of classification algorithms k-nearest-neighbor, support vector machine, random forest and neural network: A review. *Journal of Data Analysis and Information Processing* 2020;8:341–357.
- [25] Zhan Z, He X, Tang D, Dang L, Li A, Xia Q, Berto F, Li H. Recent developments and future trends in fatigue life assessment of additively manufactured metals with particular emphasis on machine learning modeling. *Fatigue Fract Eng Mater Struct* 2023;p. 1–40.
- [26] Bao H, Wu S, Wu Z, Kang G, Peng X, Withers PJ. A machine-learning fatigue life prediction approach of additively manufactured metals. *Engineering Fracture Mechanics* 2021;242:107508.
- [27] Li A, Baig S, Liu J, Shao S, Shamsaei N. Defect criticality analysis on fatigue life of l-pbf 17-4 ph stainless steel via machine learning. *International Journal of Fatigue* 2022;163:107018.
- [28] Peng X, Wu S, Qian W, Bao J, Hu Y, Zhan Z, Guo G, Withers P. The potency of defects on fatigue of additively manufactured metals. *Int J Mech Sci* 2022;221:107185.
- [29] Fatima S, Hussain A, Amir SB, Ahmed SH, Aslam SMH. Xgboost and random forest algorithms: An in depth analysis. *Pakistan Journal of Scientific Research* 2023;3:26–31.
- [30] Zhang Y, Ling C. A strategy to apply machine learning to small datasets in materials science. *Npj Computational Materials* 2018;4:25.
- [31] Voulodimos A, Doulamis N, Doulamis A, Protopapadakis E. Deep learning for computer vision: A brief review. *Computational Intelligence and Neuroscience* 2018;2018:13.

- [32] Tsopanidis S, Moreno RH, Osovski S. Toward quantitative fractography using convolutional neural networks. *Engineering Fracture Mechanics* 2020;231:106992.
- [33] Qassim H, Verma A, Feinzimer D. Compressed residual-VGG16 CNN model for big data places image recognition. In: 2018 IEEE 8th annual computing and communication workshop and conference (ccwc). IEEE, 2018 <https://ieeexplore.ieee.org/stamp/stamp.jsp?tp=&arnumber=8301729>.
- [34] Erdem F, Avdan U. Comparison of different U-net models for building extraction from high-resolution aerial imagery. *International Journal of Environment and Geoinformatics* 2020;7:221–227.
- [35] Tang K, Zhang P, Zhao Y, Zhong Z. Deep learning-based semantic segmentation for morphological fractography. *Engineering Fracture Mechanics* 2024;303:110149.
- [36] Bastidas-Rodriguez MX, Polania L, Gruson A, Prieto-Ortiz F. Deep Learning for fractographic classification in metallic materials. *Engineering Failure Analysis* 2020;113:104532.
- [37] Anidjar OH, Mega M, et al. Transfer learning methods for fractographic detection of fatigue crack initiation in additive manufacturing. *IEEE Access* 2024;.
- [38] Fang ZZ, Paramore JD, Sun P, Chandran KR, Zhang Y, Xia Y, Cao F, Koopman M, Free M. Powder metallurgy of titanium—past, present, and future. *International Materials Reviews* 2018;63:407–459.
- [39] Yap CY, Chua CK, Dong ZL, Liu ZH, Zhang DQ, Loh LE, Sing SL. Review of selective laser melting: Materials and applications. *Applied physics reviews* 2015;2.
- [40] ASTM F3001-14. Standard specification for Additive Manufacturing Titanium-6 Aluminum-4 Vanadium ELI (Extra Low Interstitial) with Powder Bed Fusion. In: *Electronics; declarable substances in materials; 3d imaging systems; additive manufacturing technologies*. West Conshohocken, PA: American Society for Testing and Materials; 2021, Volume 10.04.
- [41] ASTM E466-15. Standard practice for conducting force controlled constant amplitude axial fatigue tests of metallic materials. In: *Metals – mechanical testing; elevated and low-temperature tests; metallography*. West Conshohocken, PA: American Society for Testing and Materials; 2021, Volume 03.01.
- [42] Microsoft Corporation. Microsoft Excel, 2024. Version 365, <https://www.microsoft.com>.